Numerical Simulation of Metallic Thermal Protection System Panel Bowing

Dean A. Kontinos* and Grant Palmer[†]

NASA Ames Research Center, Moffett Field, California 94035-1000

Numerical simulation of the thermoelastic response of metallic thermal protection panels is presented. The panels, which are being designed for use on the windward surface of the X-33 flight test vehicle, deform into convex and concave bowed surfaces due to thermal gradients caused by aerodynamic heating. Three numerical models, for the flowfield, for the in-depth heat transfer, and for the thermoelastic deformation, are coupled in sequence to yield the transient response of the metallic panel. The aerothermal loads are derived from computational fluid dynamic solutions and are prescribed as a distribution function with maximum bow height as the governing parameter. Finite element models are used to simulate the thermal and structural responses. The coupled simulation is compared to a single-pass uncoupled solution. Results show negligible feedback between the structural deformation and the deformation-induced perturbation of the aerothermal heat load. Nevertheless, significant temperature variations on the surface of the panel are produced. The deformations induce lateral temperature gradients that increase the thermal stress within the panel. Finally, it is shown that panel bowing does not appreciably alter the trajectory integrated heat load.

Nomenclature

A	=	panel surface area
A_{edge}, A_1, A_2	=	distribution function parameters
D_1, E_1, E_3	=	distribution function parameters
m_{end}, m_{max}, m_{min}	=	correlation parameters
q	=	heat flux
$\bar{q}$	=	ratio of bowed surface heat flux to unbowed
r	=	distribution function
t	=	time, s
α, β	=	distribution function continuity locations
δ	=	panel bow height, in.
η	=	crossflow panel surface coordinate
ξ	=	streamwise panel surface coordinate

Subscripts

bowed	=	deformed surface
center	=	streamwise panel centerline
edge	=	streamwise panel edge
nominal	=	undeformed surface

Introduction

TO reduce the cost of inserting payload mass into low Earth orbit, the next generation reusable launch vehicle (RLV) is currently being designed by Lockheed Martin Skunk Works[1]; their lifting body configuration was selected from among three concepts for continued development. A subscale technology demonstrator, designated X-33, is being designed to flight test the advanced technologies of the RLV such as a linear aerospike engine, graphite epoxy liquid hydrogen tank, lifting body maneuverability, and a metallic thermal protection system (TPS). The X-33 is to demonstrate the integration of these technologies into an operational system capable of flying hypersonic trajectories, prove reliable seven-day reflight

capability, and provide a design database for the subsequent development of the RLV.

The survival of a vehicle operating in a hypersonic thermal environment is dependent on the TPS to maintain structural temperatures within allowable limits. Although the design of the TPS is primarily governed by mission survival, operational costs are an important design consideration. As such, the RLV and its predecessor X-33 will employ a honeycomb metallic standoff TPS concept designed by B. F. Goodrich. The anticipated advantage of a metallic TPS is its durability and maintainability. A metallic panel is inherently more rugged than ceramic insulation such as that used on the Space Shuttle. The panels are mechanically attached and, therefore, more quickly installed as compared to adhered ceramic tiles. Furthermore, the panels are designed to minimize the amount of collateral disturbance when replacing a single panel. Over the operational lifetime of the vehicle, the use of metallic panels is expected to accrue noteworthy cost savings. A discussion of design considerations of ceramic and metallic TPS is given by Jackson and Dixon.[2]

Regardless of the type of TPS, whether metallic or ceramic, the system must be designed with minimum margins of uncertainty to minimize the nonpayload weight. Therefore, it is important that the aerothermal environment as well as the in-depth conduction into the vehicle structure be predicted with sufficient accuracy throughout the flight envelope. In the instance of a standoff metallic system, the aerothermal environment and the structural response become dynamically coupled. Because the materials possess a high coefficient of thermal expansion, significant thermoelastic deformation of the panels is anticipated.[3,4] Temperature gradients through the depth of the honeycomb panel cause it to bow into the hypersonic flowfield. Modeling of the bowing phenomena is essential for accurate prediction of the performance of the metallic TPS.

Thermoelastic bowing of the metallic panels is an inherently coupled fluid–structure interaction. As opposed to aeroelasticity analysis where the surface response is from mechanical loads (pressure), the panel interaction is governed by the thermal response. During the early stages of the X-33 flight trajectory, heat is absorbed by the vehicle. As shown schematically in Fig. 1, the thermal gradient is such that the outer facesheet of the honeycomb panel is at a higher temperature than the inner sheet. Differential thermal expansion of the inner and outer facesheets cause the panel to bow outward into a convex surface. Later, as the vehicle flies through a milder aerothermal heating environment, the heat soak from earlier in the trajectory is conducted back into the flowfield. The result is a gradient inversion whereby the inner facesheet is hotter than the outer sheet. In this case, the panels deform into a concave surface shape.

*Senior Research Scientist, Eloret Thermosciences Institute. Senior Member AIAA.

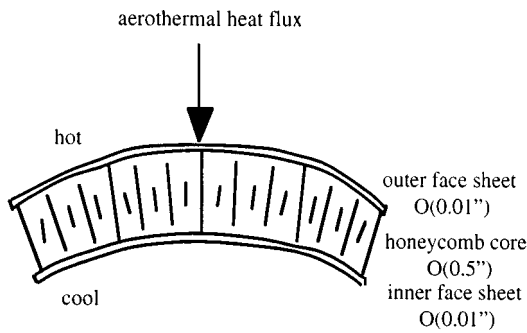[†]Research Scientist, Reacting Flow Environments Branch. Senior Member AIAA.

Fig. 1 Schematic of bowed metallic panel during period of high aerothermal heating.

Design of the metallic TPS must account for the interaction of the deformed panels and the hypersonic flowfield. In particular, the deformed panels create a quiltlike flow surface that significantly affects the local heating distribution.[5-7] Regions of augmented heating form on the windward face of the bowed panel as a function of the panel orientation, deflection height, and boundary-layer thickness. Local temperature variations must be quantified so that design margins are determined. In the event that temperatures exceed single use limits, local temperature variations may alter TPS material selection. Furthermore, the extent of the thermal penetration into the structure due to local temperature variations on the surface must be determined. In addition, the effect of local variations on the overall trajectory integrated heat load must be characterized. Another design concern is the amount of coupling between the thermoelastic deformation and the subsequent local aerothermal heating. It must be determined whether a feedback mechanism exists whereby the bowed surface configuration increases the local heating rates, thus increasing the amount of bowing. Moreover, any deformation asymmetries as a result of locally varying heating rates need to be ascertained. Previous studies[8] have demonstrated computational procedures for solving such coupled fluid–structure interactions; however, rarely are coupled analyses used to support the design of actual flight hardware for a hypersonic vehicle (see Ref. 9 for a discussion of coupling methods in hypersonic flow applications).

To address these design issues, as well as provide high-fidelity analysis in support of the design database, this paper presents a coupled simulation of the aerothermal bowing effect for the X-33 vehicle. The prediction of the flowfield, in-depth thermal conduction, and thermoelastic deformation are sequenced to provide the transient response of the metallic TPS throughout the X-33 design trajectory. The analysis is performed using a semi-empirical approach. Computational fluid dynamic (CFD) results are computed a priori to form a surface heating distribution as a function of the deflection height. This aerothermal distribution function is applied as an input load to finite element models of the TPS structure. Results are presented with a focus toward addressing the uncertainties associated with the aerothermal performance of the metallic system.

The presentation is divided into four major sections. First, the metallic TPS is described in general terms omitting specific dimensions that vary throughout the vehicle. The functionality of the TPS components are outlined in this section. Then, the three computational models are presented along with the coupling methodology. Results and analysis are presented in the next section. Finally, conclusions are given in the last section.

TPS Stackup

The X-33 TPS comprises various insulators including metallic panels, flexible blankets, and high-temperature carbon/carbon and carbon/silicon refractory composites. A brief presentation of the components of interest to this analysis is given here. As seen in Fig. 2, the outer mold line on the windward side of the X-33 is made of metallic honeycomb panels arranged in a cross-hatched configuration. The diamond shape panels are oriented obliquely to the freestream so that interpanel seal leakage is minimized. The panels are nominally 26 × 22 in. with mechanical attachments located 1.5 in. inboard from the corners. The panels are composed of ei-
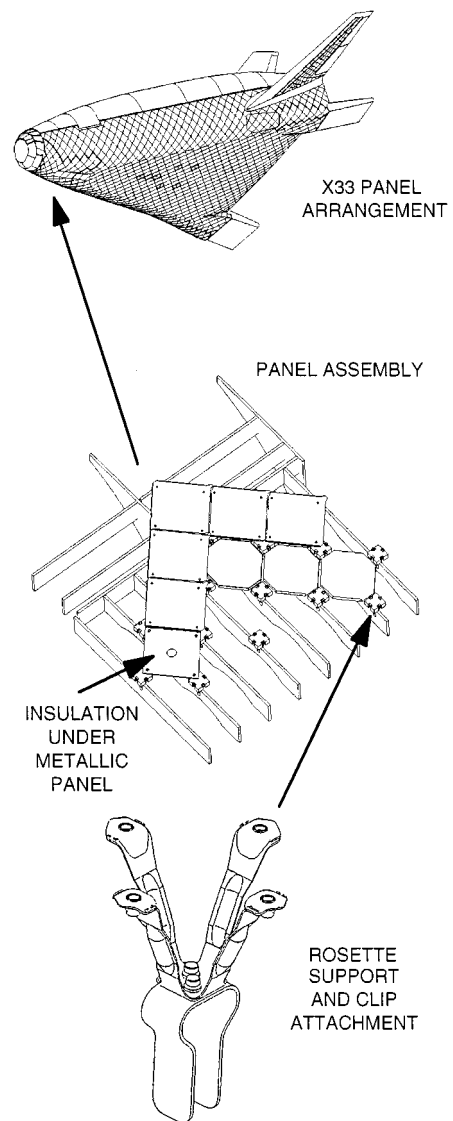

Fig. 2 X-33 metallic TPS design features.

ther PM-1000 for regions experiencing peak temperatures between 1650 and 1900°F or Inconel for cooler regions. The honeycomb is constructed of core metallic corrugations 0.006–0.01 in. thick sandwiched between facesheets of similar thickness. The edges are closed out with metallic foil. Bending stiffness is mostly provided by the facesheets. Bowing occurs when the temperatures of the two facesheets differ creating differential thermal expansion across the honeycomb.

The panels are supported by four-pronged rosettes that are fastened to the underlying TPS support structure. The rosettes are designed to absorb the thermal expansion of the panels by spreading laterally. Essentially, the rosettes are very stiff in the normal direction and possess little resistance to lateral deformation. The TPS support structure, upon which the rosette rests, is fastened to the frame of the vehicle tank structure. The TPS panels and support structure transmit the load to the tanks that are the main load-bearing members of the structure.

Thermal insulation between the hot hypersonic boundary layer and the cryofuel in the tanks is provided by the metallic panels, layers of insulation and by the separation of the TPS and tanks by the standoff design. Immediately underneath the panels is either a single layer of Q-fiber felt insulation or a double layer composed of Cerachrome insulation and Q-fiber. The insulation is encased in an Inconel foil. The thickness of the insulation is on the order of inches and varies throughout the vehicle. On the liquid oxygen (LOX) tank, a layer of 1-in.-thick SS-1171 foam insulation is applied. Although there are conduction paths through the rosette and

supporting structure, the dominant mode of heat transfer from the surface to the tank is radiation across the air gap between the underside of the TPS and the tank.

Procedure

The analysis of the bowing process is performed using three numerical models: a finite element model of the heat transfer from the surface to the tank, a finite element model of the thermoelastic deformation of the honeycomb panel, and a CFD model of the external flowfield. The models are coupled in series to provide a simulation of the transient response of the TPS system and its interaction with the flowfield.

Several assumptions about the nature of the interaction between the structure and flowfield are made. First, the quasi-steady-state assumption is made because the vibrational frequency of the panel is several orders of magnitude greater than the characteristic thermal frequency; thus, as discussed by Tauchert,[10] inertia terms may be neglected. The elastic deformation is primarily governed by the instantaneous temperature gradient across the two facesheets and, to a lesser degree, on the temperature as it affects the mechanical properties. Second, because of greatly disparate timescales, the flowfield is assumed to equilibrate instantaneously due to changes in surface shape. Thus, the flow solver produces steady-state results based on the instantaneous geometry. Last, the heat transfer through the panel is assumed to be independent of its deformation; this assumption is shown by Kontinos[9] to be valid for metallic panel configurations.

Thermal Model

The heat transfer through the structure is modeled using the commercial finite element package COSMOS/M.[11] The three-dimensional finite element thermal model (Fig. 3) is constructed to simulate the response of a typical panel located on the windward side of the X-33 immediately downstream of the nose cap. The panel is generically represented as a flat surface aligned with the flow. By assuming symmetry across the streamwise centerline, only half of the panel is modeled. The surface insulation comprises a PM-1000 metallic panel, a layer of Cerachrome, and a layer of Q-fiber. The rosette and bolt assembly are also included in the model. The bottom of the rosette is attached to a TPS support structure beam made of IM7/5250-4. Offset from the bottom of the Q-fiber is a layer of SS-1171 insulation over an aluminum LOX tank.
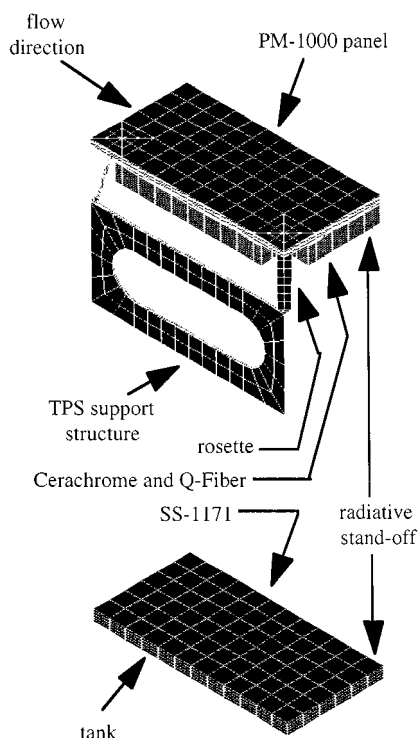

Fig. 3   Finite element thermal model of the X-33 TPS stackup.

The thermal model is composed of 2332 elements and 3552 nodes. Specific dimensions and element distributions are given in Ref. 12. Numerical experiment has shown the results with the given element density to be consistent with the results obtained using a one-dimensional heat transfer model of the same TPS stackup. All material properties used in the analysis are taken from the X-33 thermal design database, which is arranged similarly to the TPSX[13] material database.

For boundary conditions, the sides of the model are held to adiabatic conditions based on either symmetry or approximation. At the backside of the aluminum tank, a convective boundary condition is applied to simulate the evacuation of the LOX; the heat transfer coefficient is held constant while the ambient temperature is varied as a function of time. The top surface of the panel is the interface with the flowfield, where a combined convective-radiative boundary condition is applied. Per design rule, the top surface is set to radiate as a black body with an emissivity of 0.8.

Structural Model

Brick elements are used to model the in-depth thermal response. For structural analysis, however, brick elements are overly stiff in modeling a panel that behaves as a plate or shell. Thus, a separate structural model employing shell elements is created. In this analysis, sandwich shell elements provided by COSMOS are employed. The temperature gradient across the panel and the instantaneous surface temperature from the thermal model are imposed on the sandwich shell elements. The temperature gradient is the driving potential for the bowing, whereas the instantaneous temperature is needed for the temperature-dependent material properties. The same surface discretization between the thermal and structural models is used for coupling simplicity. Numerical experiment shows the panel deformation is mesh converged at densities less than the desired surface density for the thermal model. Thus, using the same surface discretization as the thermal model does not diminish the accuracy of the structural model.

The rosettes are modeled using a single effective stiffness element. The stiffness matrix is generated from a separate, high-resolution, finite element model of the rosette. In the high-resolution model, the bottom of the rosette is fixed and unit loads are applied to the panel attachment point of the rosette. By computing the resulting deflection, the effective stiffness of the rosette is ascertained. Through numerical experiment, the stiffness of the rosette is found to be insensitive to temperature; consequently, the temperature of the rosette is not transferred from the thermal model.

Fluid Dynamic Model

The flowfield is simulated using GASP[14] developed and marketed by Aerosoft, Inc. The surface boundary condition is modified to model a radiative equilibrium condition, as well as surface catalysis effects. The air is modeled as a five species reacting gas mixture (O_2, N_2, NO, N, and O) with a single temperature for the translation, rotational, and vibrational modes. Third-order Van Leer flux-vector splitting is used for the inviscid fluxes. For more on GASP and its application to X-33 CFD simulation see the paper by Prabhu et al.[15]

In this analysis, shape functions describing the surface heat distribution over a bowed surface are created based on a priori solution of the flowfield. By using the distribution functions, the perturbation to the aerothermal heating due to surface deformation is efficiently incorporated into the analysis without need for further CFD simulation. Separate distribution functions are created for convex and concave surface deformations.

In a related paper by Palmer et al.,[16] a series of axisymmetric CFD solutions are generated for flow over the forebody of the X-33. Superimposed on the surface is a series of bowed surfaces representing the metallic panels starting behind the nose cap. The bow height is varied between solutions to include both positive (convex bow) and negative (concave bow) deflections. Although not discussed in Ref. 16, also computed is a three-dimensional flowfield around the X-33 forebody with a superimposed 5 × 4 patch of spherically bowed panels located on the windward side behind the nose cap. The heat flux of the bowed surface configurations is ratioed to the nominal smooth surface values and is denoted as $q_{bowed}/q_{nominal}$. For

a panel generally aligned with the flow, the results indicate that the streamwise profile of $q_{bowed}/q_{nominal}$ along the center of the three-dimensional panel is the same shape as that over the bowed surface in the axisymmetric solution. Furthermore, the extreme values of $q_{bowed}/q_{nominal}$ are of similar magnitude for a given bow height. Subsequently, the three-dimensional solution is used to infer a general shape for $q_{bowed}/q_{nominal}$ over the surface of the panel. The axisymmetric results are then used to correlate the extreme values of the distribution as a function of the bow height. The end result is an expression for $q_{bowed}/q_{nominal}$ as a function of the position on the panel and the maximum bow height.

For the convex bowed surface, the correlation is based on CFD calculations at 35.8-deg angle of attack, Mach 11.44, and 53.4-km altitude; these are peak-heating conditions on the Mach 15 design trajectory. As shown in the data of Palmer et al.,[16] the shape of the perturbed heating profile is similar for other flow conditions, but the magnitude of the extremums differ. The magnitude of the perturbation is maximized at peak heating; thus, an element of conservatism is contained within the assumed distribution function. Also, the curve fit assumes the panel is one of several bowed panels in sequence.

The panel is given by the nondimensional coordinates ($0 \le \xi \le 1$, $-\frac{1}{2} \le \eta \le \frac{1}{2}$), where ξ is in the streamwise direction and η is in the crossflow. The bowed surface heat distribution is given by a quadratic blending of the centerline streamwise distribution obtained from the axisymmetric solutions and an edge streamwise distribution. Recall that these distributions represent the heat flux of the bowed surface ratioed to the undeformed surface. The expression is given as

$$\frac{q_{bowed}}{q_{nominal}} = 4[\bar{q}_{edge}(\xi) - \bar{q}_{center}(\xi)]\eta^2 + \bar{q}_{center}(\xi) \quad (1)$$

The centerline distribution is a blending of a quartic and a quadratic polynomial at a point α along the ξ axis. The polynomials are fit through three extreme values: the edge conditions $\bar{q}_{end}$, the peak heating value $\bar{q}_{max}$, and the minimum heating value $\bar{q}_{min}$. The centerline profile is given by

$$\bar{q}_{center}(\xi) = \begin{cases} \bar{q}_{center,1} & \text{for} \quad 0 \le \xi \le \alpha \\ \bar{q}_{center,2} & \text{for} \quad \alpha \le \xi \le 1 \end{cases} \quad (2)$$

where the individual functions are given as

$$\bar{q}_{center,1} = A_1 \xi^2 (\xi - \alpha)^2 + D_1 \xi(1 - \xi/\alpha) + \bar{q}_{end} \quad (3)$$

$$\bar{q}_{center,2} = A_2(\xi - \alpha)(\xi - 1) + \bar{q}_{end} \quad (4)$$

The edge profile is given by

$$\bar{q}_{edge} = A_{edge}\xi(\xi - 1) + \bar{q}_{end} \quad (5)$$

The coefficients are given by

$$A_{edge} = 4(\bar{q}_{end} - r m_{max}\delta - 1) \quad (6)$$

$$A_1 = [16(\bar{q}_{max} - \bar{q}_{end}) - 4D_1\alpha]/\alpha^4 \quad (7)$$

$$A_2 = \frac{4(\bar{q}_{end} - \bar{q}_{min})}{(1 - \alpha)^2} \quad (8)$$

$$D_1 = \frac{4(\bar{q}_{end} - \bar{q}_{min})}{(1 - \alpha)} \quad (9)$$

From the axisymmetric CFD solutions, the extreme values are found to vary nearly linearly with bow height and to correlate as

$$\bar{q}_{end} = m_{end}\delta + 1 \quad (10)$$

$$\bar{q}_{max} = m_{max}\delta + 1 \quad (11)$$

$$\bar{q}_{min} = m_{min}\delta + 1 \quad (12)$$

where δ is the bow height in inches. Finally, the values of the curve fit parameters are $\alpha = 0.87$, $r = 0.4$, $m_{end} = -0.5952$, $m_{max} = 0.3968$, and $m_{min} = -0.9127$.

The expression for $q_{bowed}/q_{nominal}$ over a concave bowed panel is generated following the same procedure as a convex panel. A series of axisymmetric solutions are generated over the X-33 centerline with a superimposed concave deflection pattern for various deflection depths. Also, a three-dimensional solution is generated over a portion of the X-33 that includes a 5×4 patch of deflected panels. The three-dimensional solution is used as the basis for inferring a mathematical expression for a bowed surface heating distribution, whereas the axisymmetric solutions are used to correlate extremums of the assumed distribution as a function of the bow height. All solutions are computed at conditions of Mach 8.5, 45-km altitude, and 16.4-deg angle of attack. These conditions are near the transition point from positive to negative deflection of the panel.

The panel is given by the same nondimensional coordinates as given earlier. The concave bowed surface heat distribution is given by

$$\frac{q_{bowed}}{q_{nominal}} = 4[1 - \bar{q}_{center}(\xi)]\eta^2 + \bar{q}_{center}(\xi) \quad (13)$$

The centerline distribution is a blending of two exponential functions connected by a linear distribution between points α and β:

$$\bar{q}_{center}(\xi) = \begin{cases} \bar{q}_{center,1} & \text{for} \quad 0 \le \xi \le \alpha \\ \bar{q}_{center,2} & \text{for} \quad \alpha \le \xi \le \beta \\ \bar{q}_{center,3} & \text{for} \quad \beta \le \xi \le 1 \end{cases} \quad (14)$$

where the individual functions are given as

$$\bar{q}_{center,1} = \bar{q}_\alpha + (\bar{q}_{end} - \bar{q}_\alpha)\exp[-E_1(\xi/\alpha)] \quad (15)$$

$$\bar{q}_{center,2} = \frac{[(\beta - \xi)q_\alpha + (\xi - \alpha)q_\beta]}{(\beta - \alpha)} \quad (16)$$

$$\bar{q}_{center,3} = \bar{q}_\beta + (\bar{q}_{end} - \bar{q}_\beta)\exp[-E_3(1 - \xi)/(1 - \beta)] \quad (17)$$

The parameters of the shape function are the continuity locations, α, and β, the values of the function at the continuity locations, q_α and q_β, the value of the function at the ends of the domain, $\bar{q}_{end}$, and the exponents E_1 and E_2. The continuity points α and β are chosen as 0.3 and 0.8, respectively. The end value is found to correlate with the deflection as

$$\bar{q}_{end} = 1 - 0.0655\delta \quad (18)$$

where δ is in inches and is negative in the case of a concave deflection. The remaining parameters do not correlate with the CFD data in an easily discernible way. Rather, an error minimization of the CFD results and the assumed functional form is performed over the range of deflections $-0.36 \le \delta \le 0$. The result is

$$\bar{q}_\alpha = 1 + 0.554\delta + 0.854\delta^2 \quad (19)$$

$$\bar{q}_\beta = 1 + 0.398\delta + 1.009\delta^2 \quad (20)$$

$$E_1 = 8.29 + 4.00\delta \quad (21)$$

$$E_3 = 4.24 + 1.17\delta \quad (22)$$

The heating distribution functions are based on CFD solutions computed under laminar conditions. However, turbulent heating is included in the nominal heat pulse provided by the aerothermal design database. Thus, it is assumed for this analysis that the heating distribution generated under laminar conditions is equally valid under turbulent conditions. Note that these distribution functions yield the multiplicative scale factor for the heating due to panel deflection, not the absolute magnitude of the heating. According to the experimental data of Glass and Hunt,[7] the relative increase in heating due to a surface protuberance is greater under laminar conditions than under turbulent. Therefore, using the laminar scale factor during the turbulent portion of the trajectory errs on the conservative side.
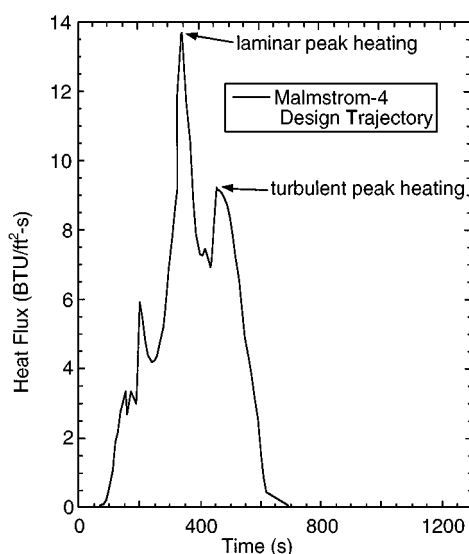
Fig. 4 Nominal surface heat flux to the X-33, windside centerline downstream of the nosecap.
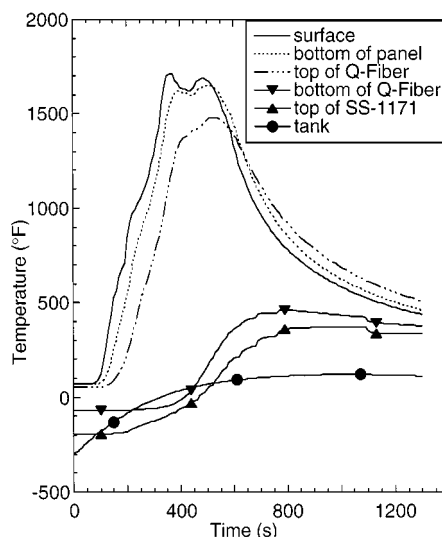

Fig. 5 Thermal response of TPS stackup from nominal surface heat flux.

Fig. 6 Panel deflection at the initial and final iteration of the coupled analysis.

Furthermore, it will be shown that both the peak heating and the peak panel deflection occur under laminar conditions; therefore, it is reasonable to assume that any difference in augmented heating due to surface deformation under laminar vs turbulent conditions is a second-order effect for this particular analysis and design trajectory. However, clearly the waviness of the surface may affect the transition to turbulence. Transition to turbulence is an important issue, but the direct inclusion of transition effects is beyond the scope of this study. The implicit assumption is that the waviness of the surface does not alter the time of transition as given by the nominal heat pulse.

Coupling Methodology

The procedure to couple the flowfield solution to the in-depth heating analysis starts with a given nominal surface heat schedule. The heat flux corresponds to the design trajectory known as Malmstrom-4 and is provided by the X-33 aerothermal database described by Bowles et al.[17] The heat pulse shown in Fig. 4 is the hot wall heat flux to the centerline of the windward side of the X-33 immediately downstream of the nose cap. This thermal load is applied uniformly over the surface of the panel, and the transient thermal response through the stackup is computed. Then, the resulting temperature distribution is used to compute the thermoelastic response of the panel. This computation provides bow height as a function of time. Employing the shape function, the nominal heating history is adjusted as a function of time and position on the panel to account for the surface deformation. In other words, at each point in time, the bow height is the single parameter that determines the bowed surface heating distribution for a given nominal heating schedule. The modified surface heat flux is used as input to the thermal model, and then the structural computation is repeated to generate an updated bowing history. This iteration process is repeated until the change in the computed deflections is less than 0.001 in. everywhere throughout the trajectory.

Results and Analysis

The heat transfer simulation is initialized at steady-state temperature conditions for the surface at 70°F and the LOX tank at −300°F. Then, the nominal heat flux is applied uniformly over the surface of the panel, and the in-depth conduction is computed for 1300 s. The computation is performed with an initial time step of 2 s for the first 20 s and then a time step of 10 s for the remainder of the simulation. Figure 5 shows the transient temperature response of the TPS at locations throughout the depth of the stackup. The in-depth temperatures are taken along a normal line down through the center of the panel. The surface temperature is seen to rise to a peak value of 1710°F at 360 s, which is 10 s beyond peak heating. The temperature then decays, followed by a second rise at 480 s. This
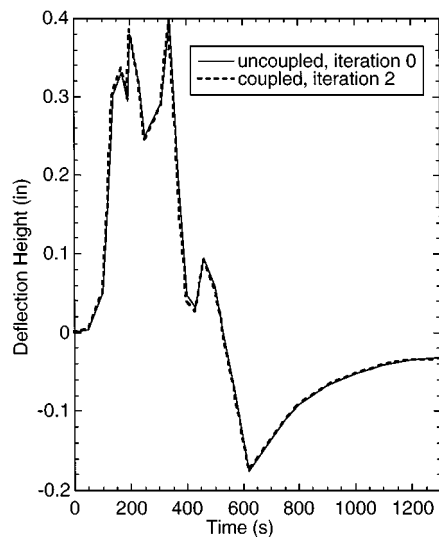
second temperature peak occurs because of transition to turbulence. Note that the peak temperatures are predicted to occur under laminar conditions. The dashed line in Fig. 5 is the back side of the honeycomb panel. It is shown to lag the surface temperature because of finite rate conduction. It is this temperature difference that drives the deformation of the panel. At 520 s, the surface and back-side panel temperatures equilibrate. As the surface heat flux is reduced, the thermal energy absorbed earlier in the flight is conducted to the surface and then radiated back into space. The temperature difference across the panel is inverted with respect to the early portion of the trajectory. Also shown in Fig. 5 are the temperature histories at the top of the Q-fiber, at the bottom of the Q-fiber, and at the top of the SS-1171 and, finally, the LOX tank temperature. The bottom of the Q-fiber and top of the SS-1171 are on opposing sides of the radiative standoff. Their temperature is primarily governed by the ambient temperature as outlined in Ref. 12. The jaggedness in the temperature profiles is a result of discontinuous change in the ambient temperature. Also, the interior tank temperature is governed by a convective boundary condition that simulates the tanks thermal response to the evacuation of the LOX. The tank begins warming in the trajectory not because of aerothermal heating but because the LOX is being pumped to the engines.

Using the earlier computed temperature history, the deflection of the panel is computed. The results of the initial elastic computation are labeled iteration 0 and are plotted as a function of time in Fig. 6. Because the supports are set 1.5 in. inboard of the corners,

the supports act as a fulcrum to the bending of the panel. The center and corners are displaced in opposite directions with respect to the support point. Thus, the deflection represented in Fig. 6 is defined as the difference of the displacement at the center of the panel and that of the corner. The deflection reaches two significant maximums of 0.38 and 0.40 in. at 200 and 340 s, respectively. The maximum at 340 s is at peak heating. The deflection curve does not directly correlate to the surface heating schedule of Fig. 4 but to the temperature difference across the panel. The temperature difference across the panel is a function of the surface heating and the conduction into the panel. Recall that a combined convective-radiative condition is applied at the surface. At low temperatures, the radiative component is small; consequently, most of the aerothermal load is absorbed by the panel thereby increasing the temperature gradient. This phenomenon is maximized at 200 s. As the temperature is increased, the radiative component increases nonlinearly, and much of the heat is rejected back into space. Thus, from 200 to 300 s the thermal gradient and subsequent deflection is reduced. Beyond 300 s, the surface heat flux increases beyond the rate at which the heat can be radiated into space. Thus, the thermal gradient is once again increased along with the deflection. This phenomenon results in the second deflection peak.

Based on the earlier defined bowed surface heating distribution, the nominal surface heat flux is adjusted in space and time to account for the deflection of the panel. A unique, adjusted heat flux is applied to each element on the panel surface in the thermal model. The thermal analysis is recomputed. The temperature results are transferred to the structural model on which the deflection is recomputed to complete an iteration. The process converges in 2 iterations, and the final iterated deflection solution is shown as the dashed line in Fig. 6. The deflection response does not change due to the surface heating perturbation caused by the bowing. The feedback between the deformation-induced heating perturbation and the bowing is shown to be negligible.

The feedback mechanism is weak because the temperature gradient across the panel is unchanged between the coupled and uncoupled analysis. Figure 7 shows the temperature difference between the top and bottom facesheets (denoted as ΔT across panel) at the center of the panel for both the nominal and coupled solutions. The finite rate conduction is insensitive to the differences in the surface heating rates resulting in similar temperature gradients.

Although the feedback of the perturbed aerothermal field to the subsequent bowing is weak, the bowing does create local temperature variations. Figure 7 also shows the temperature histories through the depth of the stackup at the center of the panel for both the nominal smooth surface and the bowed surface coupled analysis. The coupled analysis shows an increase in the surface temperature

of 100°F at 340 s due to the bowed surface shape. This increase persists through the depth of the TPS stackup to the back of the Q-fiber. An alternate view of the differences between the nominal and coupled solution is shown in Fig. 8. Here, the temperature difference between the coupled and nominal solutions is plotted as a function of time at the same points through the depth of the stackup. The maximum temperature difference occurs at 340 s, which is the maximum deflection point. The increase in temperature is seen to conduct down to the Q-fiber, which experiences an increase of 25°F at 500 s. The increase in temperature on the Q-fiber has no appreciable effect on the SS-1171.

The earlier results are shown at the panel center, which experiences increased heating due to panel bowing. However, the results at the panel center are not fully representative of the entire panel, which experiences a general perturbation over the surface. Figure 9 shows the nominal surface temperature contours at 340 s. The surface is at a fairly uniform temperature of 1650°F except at the corners, where the underlying insulation is removed to provide a path for the rosette. At the corners, heat conducts through the panel and radiates to the substructure more quickly than at the fully insulated regions of the panel. Figure 10 shows the coupled solution at the same trajectory time. Flow is from left to right. A maximum temperature of 1750°F is shown over a region covering the center of the panel skewed toward the leading edge. At the leading and trailing edges, the temperature is reduced to as low as 1400°F.

The coupled solution shows a streamwise asymmetric temperature distribution over the panel; however, this does not lead to an asymmetric bow shape. Figures 11 and 12 show the out-of-plane displacement field for both the nominal and coupled solutions. Both solutions show displacements that are similar in magnitude, as seen throughout the trajectory in Fig. 5. Furthermore, the displacement is symmetric about the panel center. Recall that the bowing is primarily governed by the temperature difference across the panel. The absolute value of the temperature affects the bowing only through

Fig. 8 Temperature difference between coupled and nominal solutions through depth of TPS stackup.
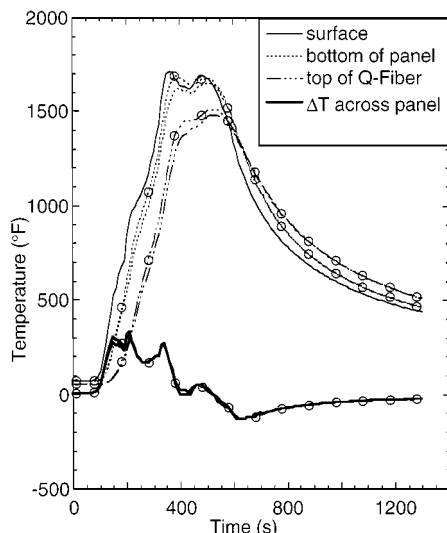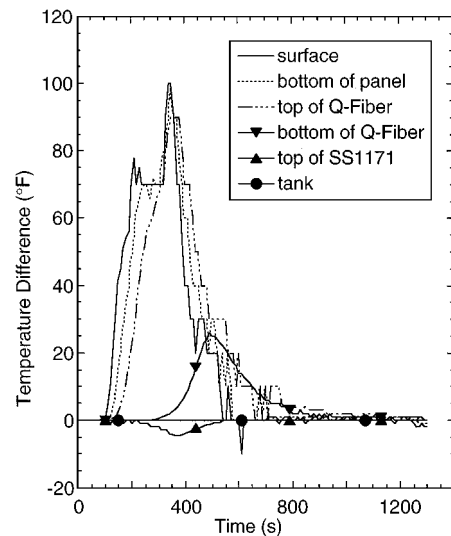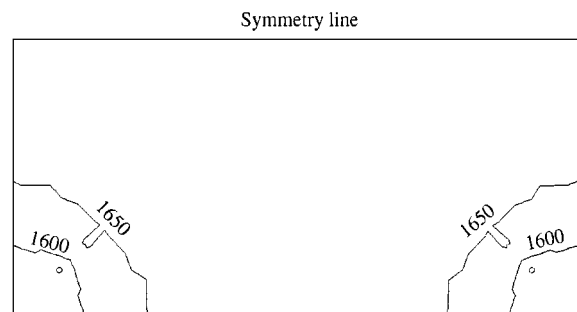

Fig. 7 Thermal response of TPS stackup from both nominal and coupled analyses; lines are the nominal results, and lines with open circles are the coupled results.

Fig. 9 Surface temperature contours (°F) over smooth surface at 340 s.

the temperature dependence of the material properties. Therefore, even though there is a large temperature variation across the panel, the temperature gradients through the panel are similar between the coupled and uncoupled solutions.

Although the spanwise surface temperature variations do not alter the out-of-plane deflection, they do affect the lateral displacement and increase the thermal stress through the panel. Figures 13 and 14 show the Von Mises stress for the nominal and coupled solutions, respectively. In the nominal case, the stress is concentrated at the rosette attachments. The coupled solution shows an increase in stress throughout the panel and, in particular, along the edges between the supports. These stresses may impact the fatigue life of the panels.

The preceding results show local temperature variations due to panel bowing. However, the results do not address the integrated effects over the surface of the panel. The surface temperature distribution of Fig. 10 suggests the potential for a change in the integrated heat load as compared to the nominal solution. For a nominal heat flux that is spatially constant over the surface of the panel, the ratio of integrated heat load is given by

$$\frac{\iint q_{\text{bowed}} \, dA}{\iint q_{\text{nominal}} \, dA} = \frac{1}{A} \iint \frac{q_{\text{bowed}}}{q_{\text{nominal}}} \, dA \qquad (23)$$
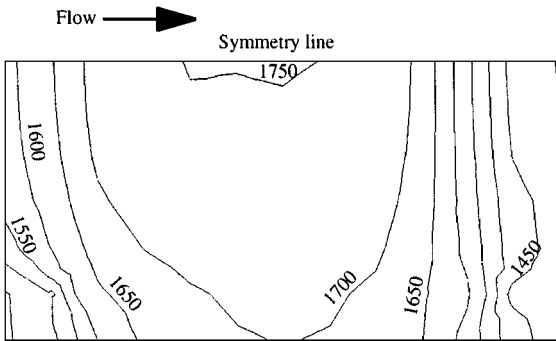

Fig. 10 Surface temperature contours (°F) over bowed surface at 340 s.
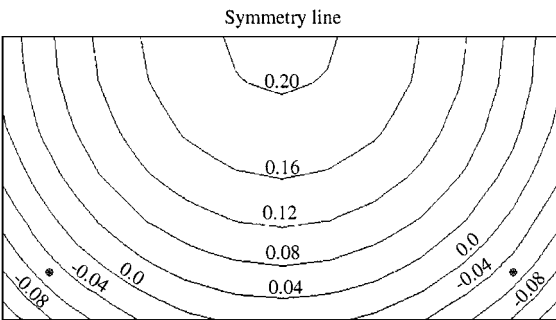

Fig. 11 Out-of-plane displacement contours (in.) at 340 s; computed using nominal heat flux.
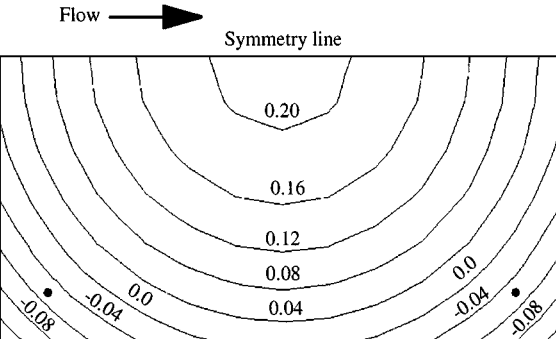

Fig. 12 Out-of-plane displacement contours (in.) at 340 s; computed using iterated heat flux.

for $q_{\text{nominal}} \neq f(A)$. The ratio of $q_{\text{bowed}}/q_{\text{nominal}}$ was specified earlier as a function of position on the panel and the bow height δ. The integrals are calculated analytically and plotted as a function of the bow height in Fig. 15. For negative deflections, the integration of the heating distribution yields a nonlinear function that shows a slight reduction in heat load over the region of deflections considered. For positive deflections, the spatially integrated heat load increases very slowly and linearly with bow height. The analytic integration yields

$$\frac{1}{A} \iint \frac{q_{\text{bowed}}}{q_{\text{nominal}}} \, dA = 1 + 0.025\delta \qquad (24)$$

Although the bowing causes significant temperature variations on the surface, the integrated heat load remains fairly constant. This
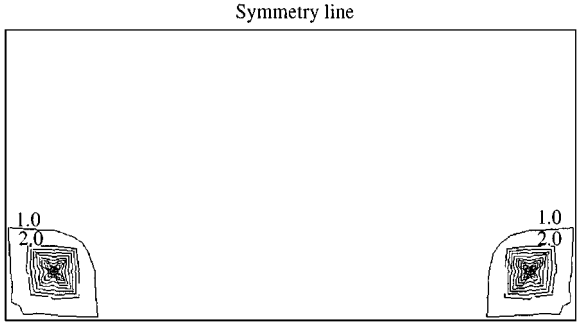

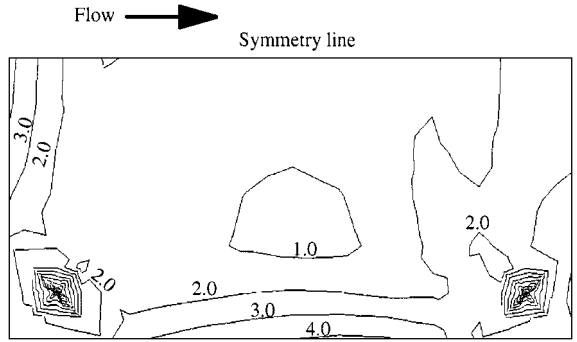**Fig. 13 Von Mises stress contours (psi $\times$ 10^{-4}) at 340 s; computed using nominal heat flux.**

Fig. 14 Von Mises stress contours (psi $\times$ 10^{-4}) at 340 s; computed using iterated heat flux.
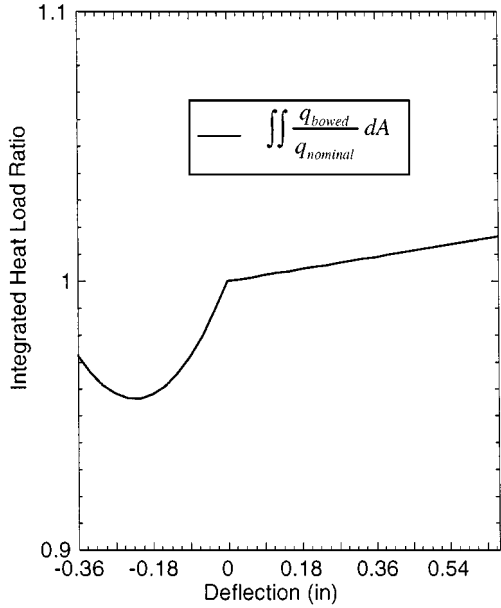

Fig. 15 Integrated heat load due to panel bowing.

result is also shown by Olsen and Smith.[5,6] Glass and Hunt[7] show a larger increase in integrated heat load due to a convex surface deformation because they consider only a single protuberance in the streamwise direction. The integrated heat load of Eq. (24) is based on a panel extracted from a series of bowed surfaces that are aligned streamwise. For a series of panels, a separation zone extends over the trailing and leading edges of tandem panels. Consequently, there is a larger region of reduced heating as compared to a single protuberance. This region of reduced heating decreases the spatially integrated heat load from that value attained over a single protuberance.

The analytic expressions are used to bound the total increase in integrated heat load over the design trajectory caused by panel bowing. Considering only positive deflection and using Eq. (24), it can be shown that the integrated heat load over time and space is given by

$$\frac{\int_0^t \iint q_{\text{bowed}} \, dA \, dt}{\int_0^t \iint q_{\text{nominal}} \, dA \, dt} = 1 + 0.025 \frac{\int_0^t q_{\text{nominal}} \delta(t) \, dt}{\int_0^t q_{\text{nominal}} \, dt} \qquad (25)$$

where $\delta(t)$ is the deflection given in inches as a function of time through the flight trajectory. As an upper bound, the deflection curve is approximated as the maximum deflection δ_{max}. The integrated heat load over time and space obeys the inequality

$$\frac{\int_0^t \iint q_{\text{bowed}} \, dA \, dt}{\int_0^t \iint q_{\text{nominal}} \, dA \, dt} < 1 + 0.025 \delta_{\text{max}} \qquad (26)$$

From Fig. 6, it is seen that δ_{max} is approximately 0.4 in. Thus, the increase in integrated heat load is less than 1% due to bowing. This small perturbation is well within design tolerances of the TPS sizing and can be neglected.

Conclusion

A numerical simulation of the thermoelastic response of the metallic TPS panels on the X-33 vehicle is presented. Distribution functions of the aerothermal heat load due to panel bowing are derived from CFD simulation. The distribution functions are coupled to finite element models of the thermal and structural response of the metallic system. A coupled solution of the thermoelastic response is generated and compared to a single-pass, uncoupled analysis.

Results of the coupled analysis show negligible feedback between the deformation-induced heat load and the panel deformation. Two factors contribute to this result. The primary factor is the perturbation in the aerothermal heat load due to panel bowing does not significantly affect the temperature gradient across the panel. The second factor is that the integrated heat load over the panel is shown to be fairly constant with bow height, and thus, the amount of thermal energy being absorbed by the panel is constant.

Nevertheless, the coupled analysis does show significant temperature variations over the surface of the panel due to bowing. An increase of 100°F is shown at peak bowing. The perturbations are shown to dissipate as the heat is conducted through the layers of insulation. Compartment and tank temperatures remain unaffected. The variation in surface temperature is shown to increase the thermal stress in the metallic panel. Finally, it is shown that the increment in integrated heat load over the entire trajectory due to panel bowing is negligible.

Unfortunately, there is no experimental data with which to compare to the present simulation. Levels of confidence can only be assigned based on the confidence in the individual analysis tools. Consequently, the simulation is checked for consistency throughout. The CFD code has been validated for external hypersonic flow applications of this type. The thermal model is compared to one-dimensional results where applicable. Also, attention is given to discretization densities to ensure grid, mesh, and time-step convergence. Levels of conservatism are applied throughout the analysis, the degree of which can not be accurately determined until comparison to flight data.

References

[1] Baumgartner, R. I., and Elvin, J. D., "Lifting Body—An Innovative RLV Concept," AIAA Paper 95-3531, Sept. 1995.

[2] Jackson, L. R., and Dixon, S. C., "A Design Assessment of Multiwall, Metallic Standoff, and RSI Reusable Thermal Protection Systems Including Space Shuttle Application," NASA TM-81780, April 1980.

[3] Gorton, M. P., Shidler, J. L., and Webb, G. L., "Static and Aerothermal Tests of a Superalloy Honeycomb Prepackaged Thermal Protection System," NASA TP-3257, March 1993.

[4] Avery, D. E., Shideler, J. L., and Stuckey, R. N., "Thermal and Aerothermal Performance of a Titanium Multiwall Thermal Protection System," NASA TP-1961, Dec. 1981.

[5] Olsen, G. C., and Smith, R. E., "Aerothermal Loads Analysis for High Speed Flow over a Quilted Surface Configuration," AIAA Paper 84-1630, 1984.

[6] Olsen, G. C., and Smith, R. E., "Analysis of Aerothermal Loads on Spherical Dome Protuberances," *AIAA Journal*, Vol. 23, No. 5, 1985, pp. 650–656.

[7] Glass, C. E., and Hunt, L. R., "Aerothermal Tests on Spherical Dome Protuberances on a Flat Plate at a Mach Number of 6.6," NASA TP-2631, Dec. 1986.

[8] Thornton, E. A., and Dechaumphai, P., "Coupled Flow, Thermal, and Structural Analysis of Aerodynamically Heated Panels," *Journal of Aircraft*, Vol. 25, No. 11, 1988, pp. 1052–1059.

[9] Kontinos, D. A., "Coupled Thermal Analysis Method with Application to Metallic Thermal Protection Panels," *Journal of Thermophysics and Heat Transfer*, Vol. 11, No. 2, 1997, pp. 173–181.

[10] Tauchert, T. R., "Thermal Shock of Orthotropic Rectangular Plates," *Journal of Thermal Stresses*, Vol. 12, 1989, pp. 241–258.

[11] "COSMOS/M Version 1.75a, Finite Element Analysis System, User Guide," Structural Research and Analysis Corp., Los Angeles, 1996.

[12] Kontinos, D. A., and Palmer, G., "Numerical Simulation of Metallic TPS Panel Bowing," AIAA Paper 98-0866, Jan. 1998.

[13] Squire, T. H., Milos, F. S., Hartlieb, G. C., and Rasky, D. J., "TPSX: Thermal Protection Systems Expert and Material Property Database," *ICCE/4, Fourth International Conference on Composites Engineering*, edited by D. Hui, International Community for Composites Engineering and College of Engineering, Univ. of New Orleans, New Orleans, LA, 1997, pp. 937, 938.

[14] "GASP Version 3, The General Aerodynamic Simulation Program, Users Manual," Aerosoft, Inc., Blacksburg, VA, 1996.

[15] Prabhu, D. K., Loomis, M. P., Venkatapathy, E., Polsky, S., Papadopoulos, P, Davies, C. B., and Henline, W. D., "X-33 Aerothermal Environment Simulations and Aerothermodynamic Design," AIAA Paper 98-0868, Jan. 1998.

[16] Palmer, G., Kontinos, D. A., and Sherman, B., "Surface Heating Effects of X-33 Vehicle TPS Panel Bowing, Steps, and Gaps," AIAA Paper 98-0865, Jan. 1998.

[17] Bowles, J. V., Henline, W. D., Davies, C. B., and Huynh, L. C., "Development of an Aerothermodynamic Environments Database for the Integrated Design of the X-33 Prototype Flight Test Vehicle," AIAA Paper 98-0870, Jan. 1998.

B. A. Bhutta
Associate Editor